4-2-2 3D Visualization and Visual Data Mining

MATSUOKA Daisuke, MURATA Ken T., FUJITA Shigeru, TANAKA Takashi, YAMAMOTO Kazunori, and OHNO Nobuaki

With the recent development of supercomputers, large scale 3D space plasma simulations to study electromagnetic environments have become practicable. We obtain a variety of 3D phenomena and configurations from 3D numerical simulations. To analyze 3D numerical simulation data has a great importance on the understanding of Earth's magnetospheric dynamics. However, it is difficult to analyze and understand 3D complex plasma phenomena or configurations. In particular, since magnetic field line's topology is strongly dependent on temporal and spatial change, it is not easy to understand time-dependent 3D configurations. In this paper, we discuss a various types of 3D visualization and Visual Data Mining(VDM) techniques to analyze the time-dependent change of magnetic field line's topology more effectively and efficiently.

1 Introduction

With the recent advancements in super-computer technologies, large-scale, high-precision, and realistic model 3D simulations have been dominant in the field of solar-terrestrial physics. Since 3D numeric data generated through simulation contain more valuable information than available in the past, innovative techniques for efficiently extracting such useful information are being required. One such technique is visualization—the process of turning phenomena, events or relations not directly visible to the human eye into a visible form. Visualizing numeric data generated by observation equipment, simulations and other means is an effective way of gaining intuitive insight into an overall picture of the data of interest.

Meanwhile, data mining is known as the art of extracting valuable information from a large amount of data relative to finance, marketing, the Internet, and natural sciences, and enhancing that information to knowledge. Data mining is defined as "extracting non-self-evident information from data"[1]. Included among the various analysis techniques available to suit specific data characteristics and objectives are pattern extraction, regression analyses, class separation and clustering. Another such technique is visual data mining intended to provide cutting-edge visualization to large volumes of data that are difficult to understand when visualized in a simple manner, thereby allowing heuristic analysis[2].

Techniques aimed at analysis data in a 2D plane, such as wavelet analyses and pattern recognition, are commonly known means of applying visual data mining to numerical simulation data in the fields of natural sciences. Conversely, visualization and data mining techniques that target data in a 3D space have yet to be established regarding the extraction of information from 3D data. We have thus pursued visual data mining techniques capable of extracting information from 3D data and 3D time-varying data, and analyzing it heuristically. In this paper, we introduce various techniques for visual data mining for 3D time-varying data

generated from 3D simulations for solar-terrestrial physics, and related applications.

This paper is organized as follows: Section **2** introduces the 3D visual data mining environment used in a series of studies; Section **3** describes the magnetospheric MHD simulation for generating magnetic flux ropes—a key subject of analysis in this paper; Section **4** classifies the features of the 3D topology of magnetic field lines in a magnetic flux rope, and estimates related time-dependent changes; Section **5** extracts the possible sites of magnetic reconnection based on estimation results given in Section **4**; and Section **6** summarizes the findings of this work and presents their future perspectives.

2 3D visual data mining

2.1 Knowledge discovery process and dataflow model

Visual data mining is a process dedicated to discovering scientific knowledge of interest from numeric data. Figure 1 shows the general flow of knowledge discovery, including data mining. The researcher selects the data to be analyzed, and then preprocesses, transforms or otherwise manipulates that data as needed. Then the researcher performs data mining on the data to evaluate the results. This sequence of processes is repeated based on the evaluation results to ultimately enhance the data to knowledge. In the knowledge discovery process, a key to discovering better knowledge is being able to feed back the results of evaluations conducted by humans and any known information to the knowledge discovery process with greater ease and in a more interactive manner.

Figure 2 shows a model of the flow of processing and data (dataflow) in the visualization process. The researcher selects time steps, physical components and other elements as the objects of analysis from numerical data,
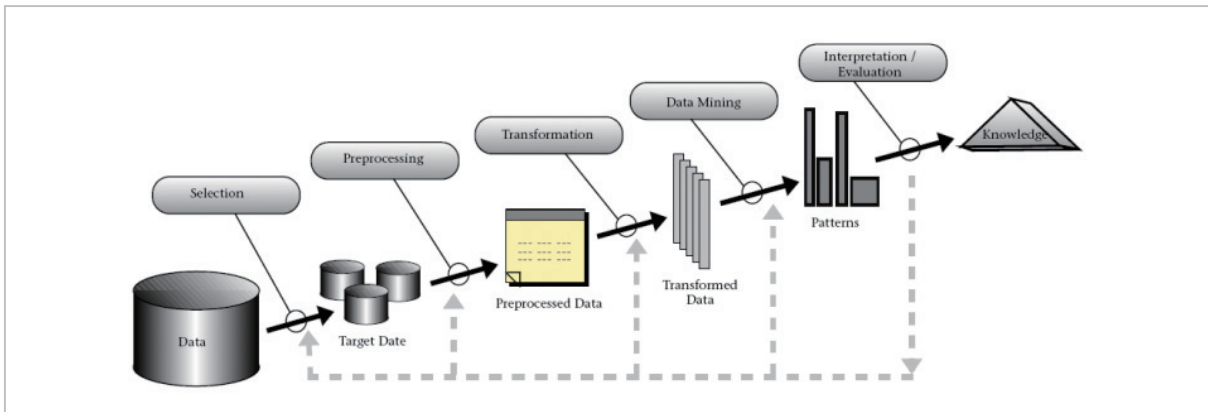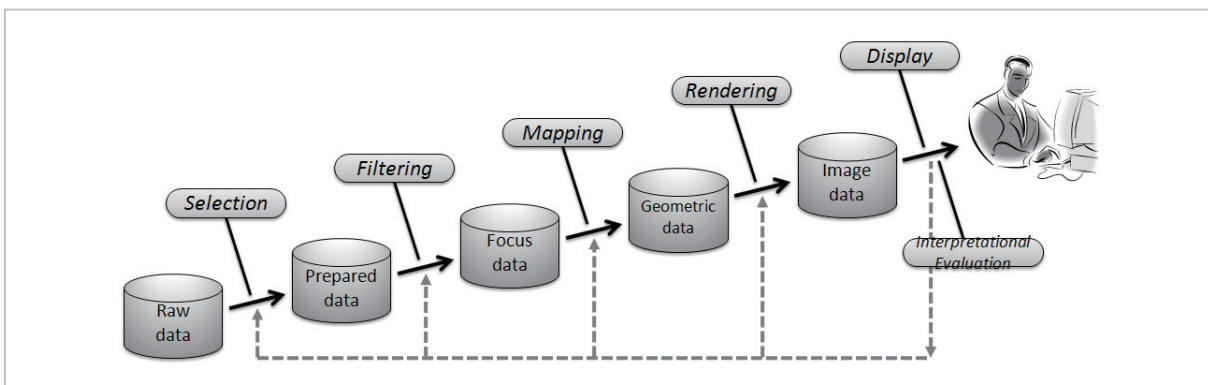

Fig.1 *Knowledge Discovery Process* [1]

Fig.2 *Visualization Dataflow Model* [3]

and then filters the data as needed, such as by reduction. Next, filtered discrete data in 3D space is transformed into geometric data, such as isosurfaces and stream lines. Since this geometric data is 3D data, it is rendered to generate image data with an eye direction and eye position being set. The analysis process may be pursued interactively with the eye position and visualization technique being modified, and data selection repeated as needed. Because the visualization dataflow model is similar to an intellectual discovery process, the data mining process used in the intellectual discovery process is replaced by visualization. Visualization-based data mining is characterized by how easy human knowledge and information can be interactively assigned to the knowledge discovery process.

2.2 3D visual data mining environment

In the visual data mining process, human interactions occur between the understanding and feedback of results. More specifically, these interactions include a visual perception of the visualization results, the selection of physical components, parameters, regions, visualization techniques, eye position and more. Flat displays, mouse devices, keyboards and other equipment have traditionally been used as computer interfaces for these operations. It is difficult, however, to output stereo video or input 3D positions with such interfaces.

In this work, portable VR [4] and CAVE [5] are therefore used as virtual reality systems capable of producing stereo video output. PHANToM [6] and a Wanda [7] have also been used as 3D pointers to positioning in 3D space. CAVE, in particular, offers an augmented sense of immersion thanks to its four- (or five-sided) configuration as shown in Fig. 3. CAVE may be coupled with a head mount display (HMD) or Wanda that allows for spatial localization to offer an enhanced level of operational interactivity. As shown in Fig. 4, PHANToM allows not only 3D spatial positions to be specified, but also the conversion of data into a sense of touch or force for feed-
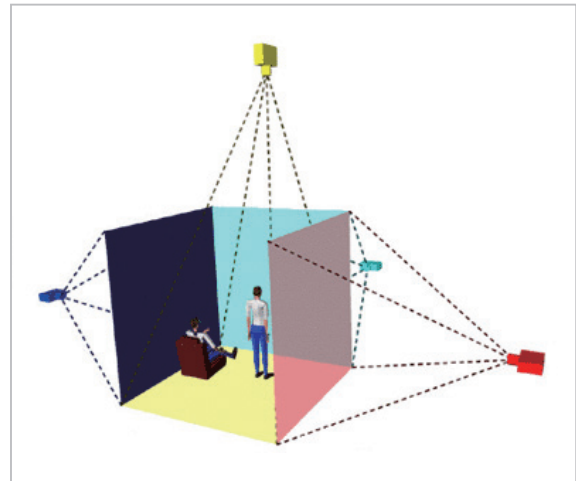

Fig.3 CAVE [5]

Fig.4 PHANToM [6]

back. This work has been conducted by using CAVE in combination with a Wanda to gain an overall picture of 3D visual mining data, as well as portable VR with PHANToM for detailed data analysis.

3 3D global MHD simulation for magnetic flux rope generation

3.1 3D global MHD simulation

A 3D global MHD simulation has been conducted with a view to analyze interactions between solar wind and the interplanetary magnetic field (IMF), and the Earth's magnetosphere. This simulation code [8] has been used in which an MHD equation approximating the particles that comprise plasma as a fluid is differentiated by using a TVD scheme.

Figure 5 shows a grid-point model having a non-orthogonal structure (GSM coordinate system) consisting of deformed spherical coordinates. It has 88 grid points in the latitude direction, 120 in the longitude direction, and 120 in the vertical direction (with each grid point count reduced to 1/10 in the diagram), along with tight grid points in the tail.

3.2 Input parameters

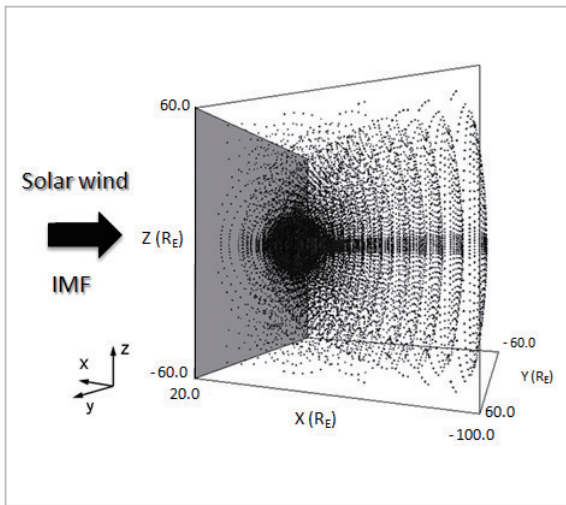Observation data on solar wind (e.g., x-component of velocity, temperature, density)

and the IMF (B_Y, B_Z) observed by the satellite ACE have been used as input parameters. These parameters are assigned uniformly from the upstream region (x=20R_E) of the magnetosphere as shown in Fig. 5. Figure 6 shows a plot of the B_Y and B_Z components of the input parameters used. The northward IMF at time (a) having an intense B_Y component is initially assigned to the magnetic dipole in order to generate a steady-state magnetosphere, with the IMF suddenly turning southward at time (b).

3.3 Simulation results

Figures 7 and 8 show the simulation results. Figure 7 shows 3D visualization results of time-dependent changes in the iso-surface of plasma pressure as viewed from the tail on the duskside. Figure 8 shows time-dependent changes in the magnetic field lines viewed from the same direction as in Fig. 7, where these changes are visualized with 120 starting points placed at intervals of 1R_E on the x-axis. Figure 7 also shows a plasma sheet drawn thinly over the time lapse, with a mass of plasma separated from the plasma sheet propagating toward the tail of the magnetosphere. Likewise, Fig. 8 shows evidence that the helical magnetic field lines in the mass of
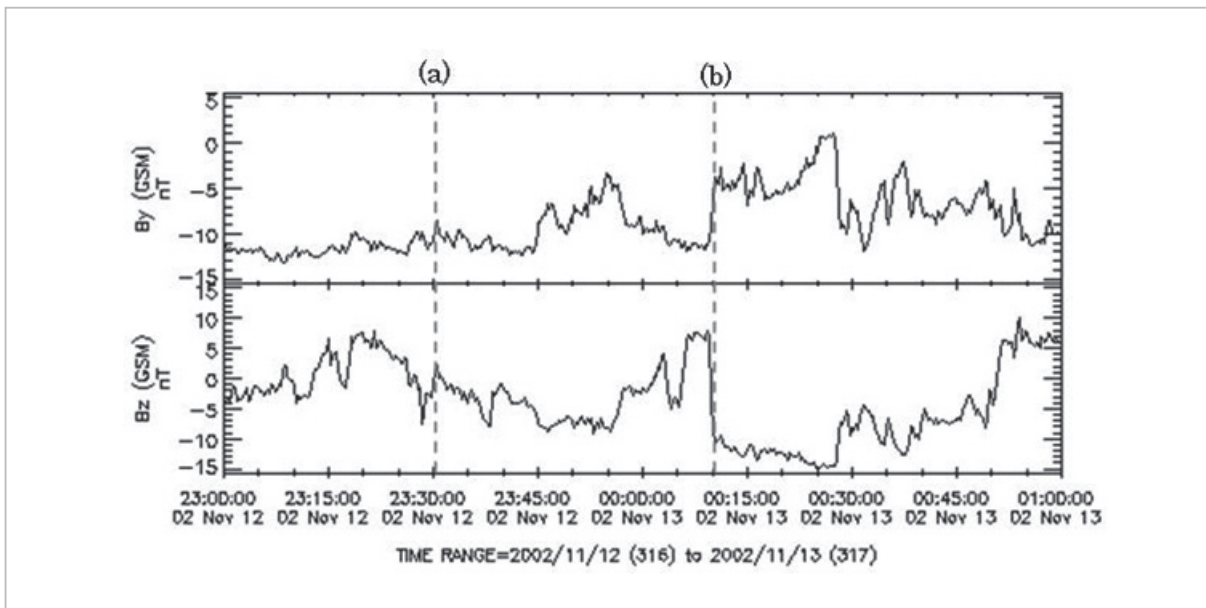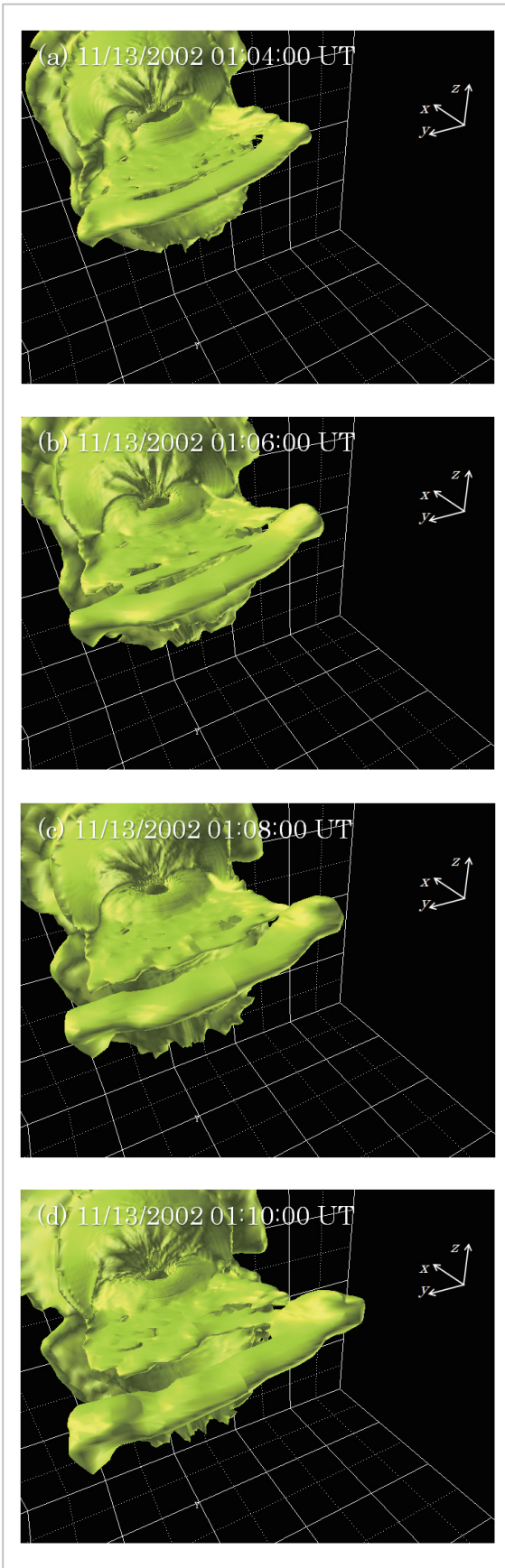
Fig.6 Input Parameters

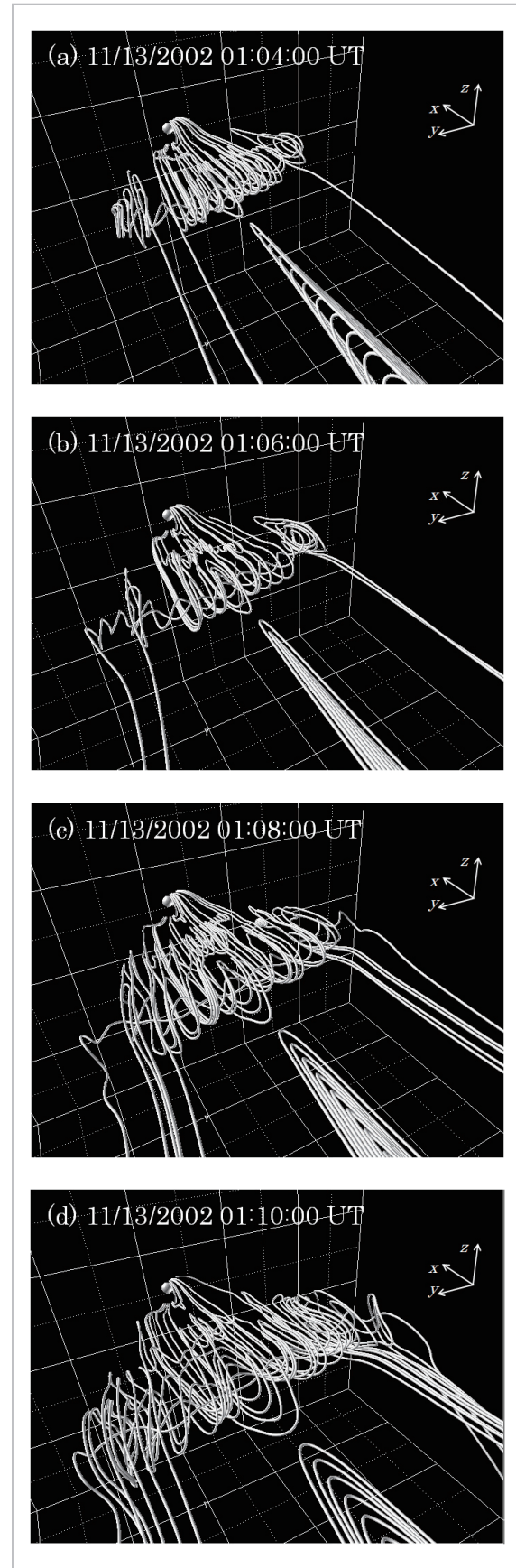**Fig.7** *Time-Dependent Changes on Iso-surface of Plasma Pressure*

Fig.8 *Time-Dependent Changes in Magnetic Field Lines*

plasma propagating toward the tail of the magnetosphere have evolved significantly into a loop known as a "magnetic flux rope".

It is known that energy is released in the magnetotail when the southward IMF suddenly turns northward. A mass of high-density, high-pressure plasma having a loop or helical magnetic field structure is generated at this time[9][10]. This is called a "plasmoid" or "magnetic flux rope" (depending on characteristics of the magnetic field structure). A magnetic flux rope as shown in Fig. 8 is known to be generated, especially when the IMF has an intense B_Y component as in the input parameters used in this work. This fact has also been confirmed through artificial satellite observations and numeric simulations[11]-[13].

4 Analysis of time-dependent changes of magnetic flux ropes

4.1 Structural classifications of magnetic flux ropes

In this section, we describe a visual data mining technique designed to understand the magnetic field topology associated with time-dependent change of a magnetic flux rope. A magnetic flux rope is known to be generated

in the tail of the terrestrial magnetosphere as the IMF reconnects to the geomagnetic field on the front of the terrestrial magnetosphere upon occurrence of flux transfer events (FTEs), and is then disconnected from the geomagnetic field over the time lapse to connect to the IMF[14][15]. However, detailed changes in magnetic field topology during the processes of generating, propagating, and then disconnecting a magnetic flux rope from the geomagnetic field have yet to be elucidated.

In this work, we first categorized the magnetic field topology in all time steps in an effort to understand the 3D structure of a mag-
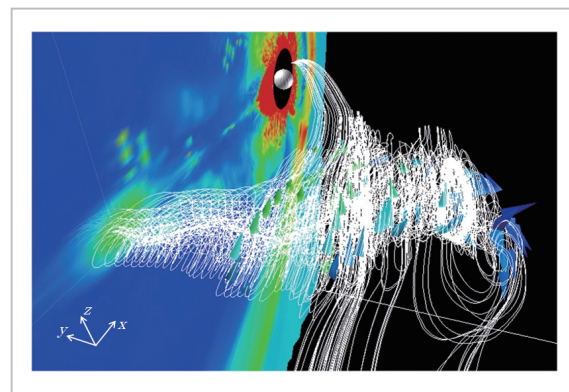

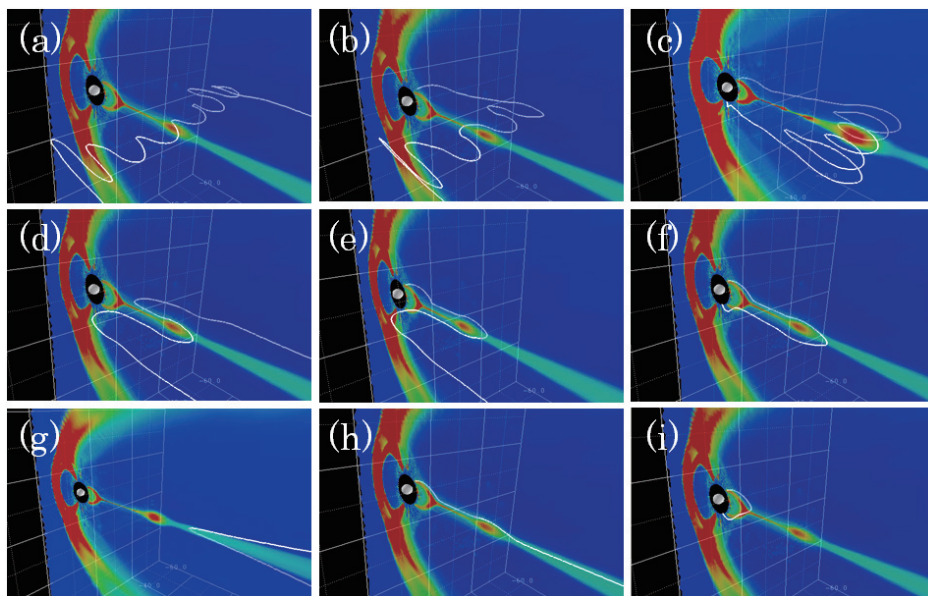Fig.9   Particle Traces along Magnetic Lines of Force

Fig.10   Structural Categorization of Magnetic Flux Ropes

netic flux rope. To identify the characteristic topology from complicated bundles of magnetic field lines, the magnetic field lines in the magnetic flux rope were visualized by using particle traces in those lines from the meridian plane. Figure 9 shows a view of particle tracing along the magnetic field lines from the meridian plane. A visual understanding of the characteristics of particle traces can be attained by discharging massless test particles along the velocity field[16]. CAVE and a portable VR system were also used in combination to gain more intuitive insight into the 3D structure of magnetic flux rope.

Figure 10 shows the 9 kinds of magnetic field topology consequently identified as follows: (a) detached (helical), (b) open (helical), (c) closed (helical), (d) detached (non-helical)), (e) open (non-helical), (f) closed (non-helical), (g) detached (not flux rope), (h) open (not flux rope) and (i) closed (not flux rope). Magnetic field topology is broken down into three broad categories: open (topology where one end of each magnetic field line contacts the earth, with the other contacting the IMF), closed (topology where each magnetic field line contacts the earth at both ends), and detached (topology where each magnetic field line contacts the IMF at both ends). Each category of magnetic field topology is further divided into three kinds: helical (helical magnetic flux rope), non-helical (non-helical magnetic flux rope), and non-flux rope (surrounding of a magnetic flux rope).

4.2 Time-dependent changes in magnetic field topology

We then analyzed how the 9 kinds of magnetic field topology vary over the time lapse. In this work, the magnetic lines of force passing over the grind points placed at intervals of 0.1 IR_E in the meridian planes of $-30R_E \leq x \leq -10R_E$ and $-2R_E \leq z \leq 2R_E$ as shown in Fig. 11 were treated using the categorization results in Fig. 10 for automatic categorization. The visualization result of each magnetic field line was projected in the xy and xz planes, and the pixels of image data were scanned to discriminate a loop count for the magnetic field line. In the xz plane, scanning was done by using 8 lines extending radically from the center point of the magnetic flux rope as shown in Fig. 12 (a). The magnetic field topology was classified as (a) through (c) when the average number of intersections of each scan line with
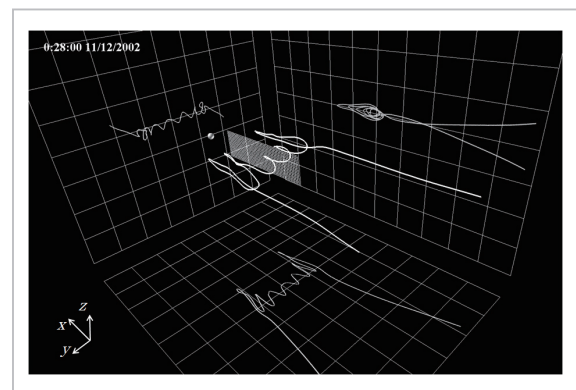

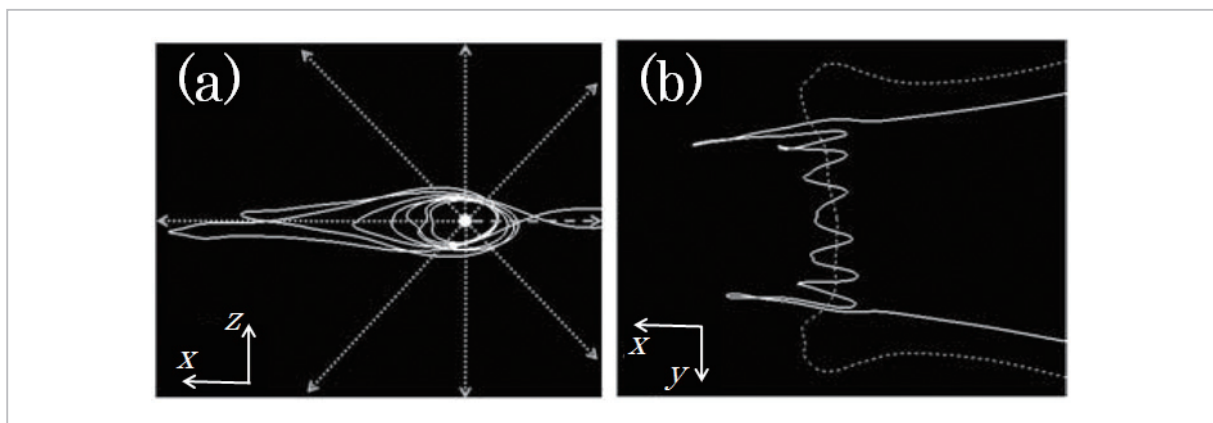
Fig.11 Projection of Magnetic Field Lines in a 2D Plane

Fig.12 Automatic Categorization of Magnetic Field Topology using Projected Images
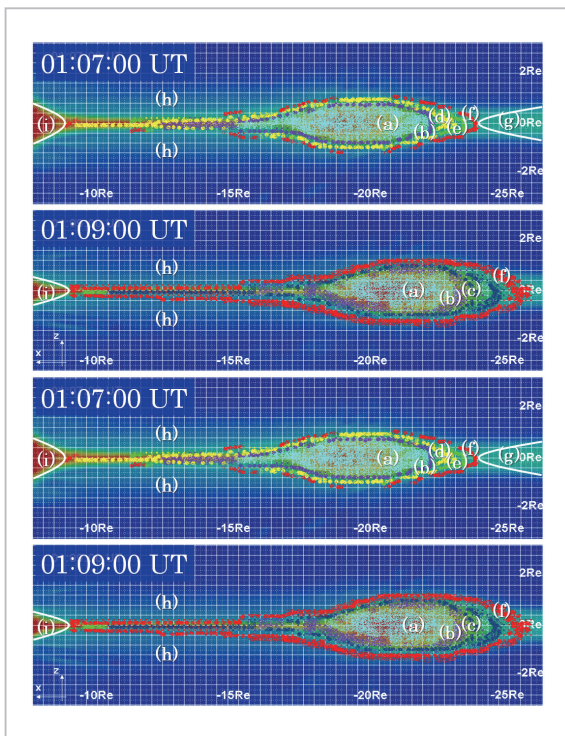
Fig.13 *Time-Dependent Changes in Topology Distributions*

the magnetic field line was less than 1, (d) to (f) when 1 to less than 3, and (g) to (i) when 3 or more. In the xy plane, each magnetic field line was also distinguished as being open, closed or detached (Fig. 12 (b)), depending on its end positions. With all these results being combined, the magnetic field lines were classified as one of the 9 kinds of magnetic field topology.

Discriminating the features of image data projected in a 2D plane can be more cost-efficient in terms of the calculation process than plotting magnetic field lines from 3D data. The discrimination process can be automated to allow the classification of more magnetic field lines, thereby enabling a more detailed analysis.

Figure 13 shows time-dependent changes in magnetic field topology in the meridian plane from 01:07:00 UT to 01:13:00 UT, as calculated using the aforementioned technique. Most of the magnetic flux rope consisted of helical detached magnetic field lines (a) at 01:07:00 UT, on the outside of which are helical open magnetic field lines(b), non-heli-

cal magnetic field lines (d), non-helical open magnetic field lines (e), and non-helical closed magnetic field lines (f). Open magnetic field lines (h) in the rope region exist outside of all these magnetic field lines. At 01:09:00 UT, the non-helical detached magnetic field lines (d) and non-helical open magnetic field lines (e) that used to exist at 01:07:00 UT disappeared, being replaced by helical closed magnetic field lines(c). At 01:11:00 UT, the magnetic field lines appeared in the same order as at 01:09:00 UT, but with increased proportions of helical detached magnetic field lines (a) and the magnetic flux rope. A trend similar to that observed at 01:11:00 UT was also noted at 01:13:00 UT.

As a result of tracking changes in topology distributions along the velocity field, the magnetic flux is estimated to have increased in diameter, with widening internal topology distributions over the time lapse. Hence, topology distributions are found to have changed in the following order: (h) or (g) to (f), ((e), (d)), (c), (b), and (a).

5 Magnetic reconnection in time-dependent changes in magnetic flux ropes

The changes in magnetic field topology estimated in Section **4.2** are verified by visualizing the magnetic field lines. PHANToM—an input interface in 3D space—has been used to interactively specify the starting points for drawing magnetic field lines. As a result, the 5 kinds of changes in magnetic field topology as described below have been verified.

First, the IMF having a B_Y component initiates reconnection to the geomagnetic field at the dayside of the magnetosphere as shown in Fig. 14 (a) to generate an open magnetic field line as shown in Fig. 14 (b). The open magnetic field line generated in Fig. 14 (b) then reconnects with the closed magnetic field line having a By component, causing a detached magnetic field line (or open magnetic field line linked to the IMF at one end) originating from the IMF to sneak into magnetosphere as

shown in Fig. 14 (c). This magnetic field line becomes a core field line in the magnetic flux rope. Prior studies have demonstrated similar topological changes[13][15][17].

In order for the magnetic field line linking to the IMF at both ends as generated in Fig. 14 to become a core field line in the magnetic flux rope, the core field line must be enclosed by closed magnetic field lines. If the rope magnetic field across the core field line is
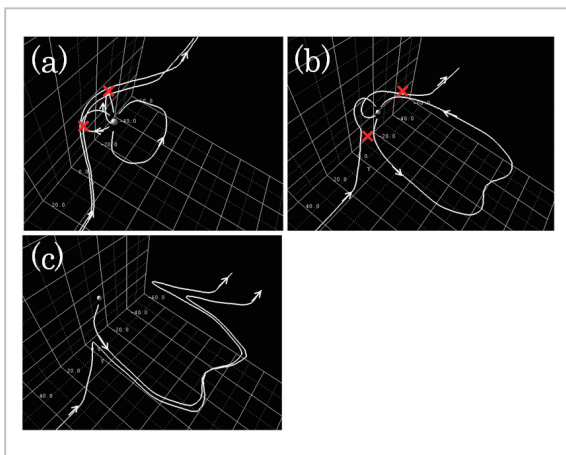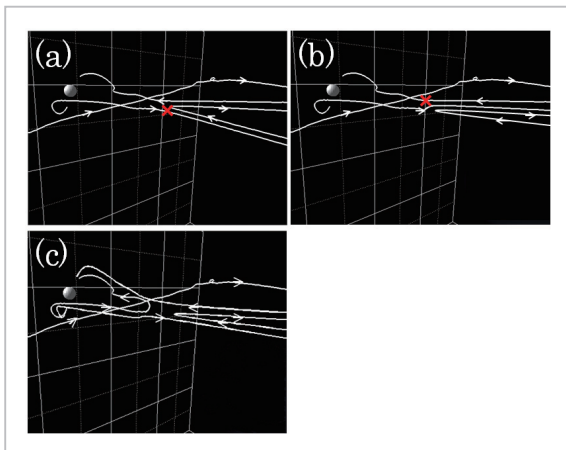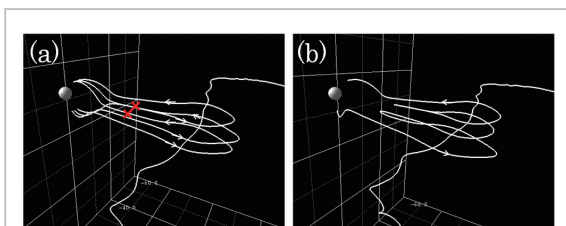
reconnected in the tail of the core field line as shown in Fig. 15, the magnetic field line to become a core field line can sneak inside a closed magnetic field line. Such reconnection of magnetic field lines occurs uniformly in the dawn to dusk direction, rather than at a single location.

The reconnection shown in Fig. 15 generates a closed magnetic field line, thereby enclosing the magnetic field line that serves as a core field line. The uniform occurrence of such reconnection in the dawn to dusk direction produces the state shown in Fig. 16 (a). Since the magnetic field line in the magnetosphere has an intense B_Y component under the influence of IMF B_Y, the closed geomagnetic field is likewise inclined with a B_Y component. Consequently, the inclined geomagnetic

Fig.14   Generating a Core Field Line

Fig.15   Capturing a Core Field Line

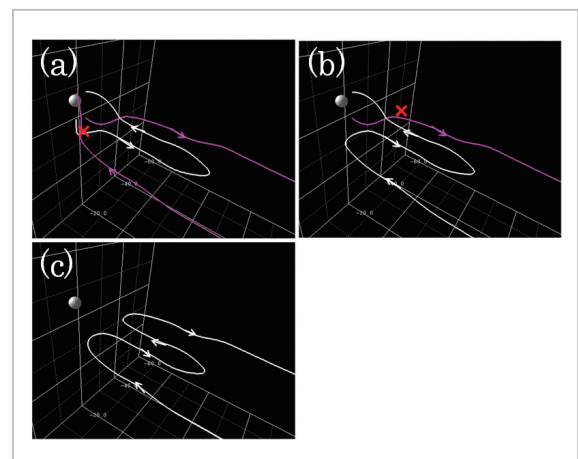
Fig.16   Generating a Helical Magnetic Field Line
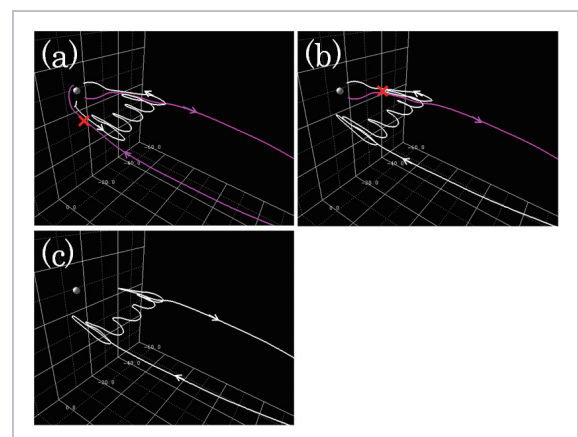

Fig.17   Reconnecting from Geomagnetic Field (1)

Fig.18   Reconnecting from Geomagnetic Field (2)

fields reconnect at the location shown in Fig. 16 (a). Because this reconnection occurs not only at a single location but uniformly in the dawn to dusk direction, a closed magnetic flux rope like that shown in Fig. 16 (b) is generated.

The closed geomagnetic field that encloses the magnetic flux rope reconnects to an open helical magnetic field as shown in Fig. 17, thereby turning into a detached magnetic field line. The closed magnetic flux rope reconnects to the open helical magnetic field as shown in Fig. 18, in order to disconnect from the geomagnetic field.

6 Conclusions

In this paper, we introduced typical applications of visual data mining aided by the use of various 3D visualization techniques with reference to magnetic flux rope - a complex magnetic structure observed in the magnetosphere. We gained insight into 3D structures, particularly with the aid of the 3D I/O interfaces of CAVE and PHANToM, and also achieved highly interactive visualization processing performance. Moreover, the visualization results were subjected to imaging operations to cut calculation costs, along with the batch-processing of large volumes of visualization results to analyze spatiotemporal changes with higher precision. We now look to the 3D visualization of separatrix surfaces using super-spatiotemporal resolution data and time-trace magnetic field lines, with a view toward developing more detailed insight into the 3D distributions and time-dependent changes in magnetic field topology.

Recent years have witnessed a wider availability of supercomputers offering computing capability surpassing PFLOPS, calling for reform not only in simulation technologies but also the techniques for visualizing and analyzing resultant data sets. Next-generation space weather prediction should benefit from the visualization of a large amount of numeric data into a form easily understood by humans, while feeding back results to the visualization process as knowledge, in order to proceed with efficient analysis.

References

1 W. Frawley, G. Piatetsky-Shapiro, and C. Matheus, "Knowledge Discovery in Databases: An Overview," AI Magazine Fall 1992, pp. 213–228, 1992.

2 D. A. Keim, "Information Visualization and Visual Data Mining," IEEE Transactions on Visualization and Computer Graphics, Vol. 8, No. 1, pp. 1–8, 2002.

3 R. B. Haber and D. A. McNabb, "Visualization idioms: A conceptual model for scientific visualization systems," Visualization in Scientific Computing, pp. 74–93, IEEE Computer Society Press., 1990.

4 Portable VR, http://www.jip.co.jp/si/soft/avs/App/pvr.html, 2003.

5 C. Cruz-Neira, D. J. Sandin, T. A. DeFanti, R. V. Kenyon, and J. C. Hart, "The CAVE: Audio Visual Experience Automatic Virtual Environment," Communications of the ACM, Vol. 35(6), pp. 64–72, 1992.

6 PHANToM, http://www.sensable.com/haptic-phantom-omni.htm, 2003.

7 Wanda, http://www.ascension-tech.com/realtime/WANDA.php, 2002.

8 T. Tanaka, "Three dimensional magnetohydrodynamic simulation on the unstructured system using the finite volume TVD scheme," Computational Fluid Dynamics Journal, 1, 14, 1992.

9 E. S. Hones Jr., "The magnetotail: Its generation and dissipation," in Physics of Solar Planetary Environments, edited by D. J. Williams, pp. 558–571, AGU, Washington, D. C., 1976.

10 E. S. Hones Jr., "Plasma flow in the magnetotail and their relation to substorms theories," in Dynamics of the Magnetosphere, edited by S. I. Akasofu, p. 545, AGU, Washington, D. C., 1979.

11 C. T. Russell, and R. C. Elphic, "Observation of magnetic flux ropes in the Venus ionosphere," Nature, 279, pp. 616–618, 1979.

12 W. J. Hughes and D. G. Sibeck, "On the 3-dimensional structure of plasmoids," Geophysical Research Letter, 14, 636, 1987.

13 T. Ogino, R. J. Walker, and M. Ashour-Abdalla, "A global magnetohydrodynamic simulation of the response of the magnetosphere to a northward turning of the interplanetary magnetic field," Journal of Geophysical Research, Vol. 99, No. A6, pp. 11027–11042, 1994.

14 A. Ieda, D. H. Fairfield, T. Mukai, Y. Saito, S. Kokubun, K. Liou, C.-I., Meng, G. K. Parks, and M. J. Brittnacher, "Plasmoid ejection and auroral brightnings," Journal of Geophysical Research, Vol. 106, No. A3, pp. 3845–3857, 2001.

15 J. C. Dorelli and A. Bhattacharjee, "On the generation and topology of flux transfer events," Journal of Geophysical Research, 114, A06213, doi: 10.1029/2008JA013410, 2009.

16 D. Matsuoka, K. T. Murata, S. Fujita, T. Tanaka, K. Yamamoto, and E. Kimura, "Analyses of 3D Structure of Magnetic Flux Ropes via Global MHD Simulations," Transaction of the Visualization Society of Japan, Vol. 28, No. 6, pp. 38–46, 2008.

17 T. Tanaka, "Configuration of the magnetosphere-ionosphere convection system under northward IMF condition with non-zero IMF By," Journal of Geophysical Research, 104(A7), pp. 14,683–14, 690, 1999.

MATSUOKA Daisuke, *Ph.D.*

Research Scientist, Earth Simulator Center, Japan Agency for Marine-Earth Science and Technology

Solar-Terrestrial Physics, Scientific Visualization

MURATA Ken T., *Ph.D.*

Group Leader, Space Environment Group, Applied Electromagnetic Research Center

Information Communication Technology

FUJITA Shigeru, *Dr. Sci.*

Associate Professor, Meteorological College

Physics of the Magnetosphere-Ionosphere System

TANAKA Takashi, *Dr. Sci.*

Professor, Graduated School of Sciences, Kyushu University

Magnetospheric Compound System Physics

YAMAMOTO Kazunori

Research Student, Fuclty of Engineering, Ehime University

Virtual Observation, Semantic Web

OHNO Nobuaki, *Ph.D.*

Research Scientist, Earth Simulator Center, Japan Agency for Marine-Earth Science and Technology

Scientific Visualization, Virtual Reality